

DOUBLE MRF FOR WATER CLASSIFICATION IN SAR IMAGES BY JOINT DETECTION AND REFLECTIVITY ESTIMATION

Sylvain Lobry^{1,3*}, Loïc Denis², Florence Tupin¹, Roger Fjørtoft³

¹LTCI, Télécom ParisTech, Université Paris Saclay, Paris, France

²Univ Lyon, UJM-Saint-Etienne, CNRS, Institut d'Optique Graduate School, Laboratoire Hubert Curien
UMR 5516, F-42023, Saint-Etienne, France

³Centre National d'Etudes Spatiales, 31400, Toulouse, France

ABSTRACT

Classification of SAR images is a challenging task as the radiometric properties of a class may not be constant throughout the image. The assumption made in most classification algorithms that a class can be modeled by constant parameters is then not valid.

In this paper, we propose a classification algorithm based on two Markov random fields that accounts for local and global variations of the parameters inside the image and produces a regularized classification. This algorithm is applied on airborne TropiSAR and simulated SWOT HR data. Both quantitative and visual results are provided, demonstrating the effectiveness of the proposed method.

Index Terms— SAR, Classification, SWOT, MRF

1. INTRODUCTION

Thanks to their interferometric potential and their ability to acquire images independently of the weather conditions or solar illumination, SAR sensors are particularly popular. In the Surface Water and Ocean Topography (SWOT) mission jointly led by NASA's Jet Propulsion Laboratory (JPL) and the French space Agency, *Centre National d'Études Spatiales* (CNES), the main instrument is a Ka-band Radar Interferometer (KaRIn). It will allow for repetitive measurements of the height of the earth's water surfaces [1]. Other applications of SAR images include mapping, change detection and crop monitoring. One of the first steps in these applications is a classification of the image. This can be achieved at the pixel level [2] or after a segmentation of the image. For instance, in [3], the segmentation is performed using an anisotropic diffusion on the filtered image and by applying an adaptive threshold to suppress unwanted edges. A local threshold is then applied to separate between the classes. In [4] the segmentation is done using level-sets with the probability density functions estimated using the Expectation-Maximization algorithm. In [5], a non-local active contour model is applied in order to account

for some variations in the radiometry of the object. Finally, it can be achieved using the Markov Random Fields (MRF) framework, as in [6].

In the context of the SWOT mission, classification to separate water from land is a preliminary step toward height estimation in these areas. Given the high frequency used by KaRIn (35.6 GHz, 0.85cm) and the near-nadir incidence angle ($1-4^\circ$), most water areas are expected to backscatter the radar pulse, whereas rougher surfaces (such as land) will appear dominated by the thermal noise. The very specific operating mode of KaRIn prevents from efficiently performing the correction of the antenna pattern, which is usually done during SAR processing (see [7] for the case of TerraSAR-X): the evolution through the swath depends on the class (*i.e.*, water or land). Moreover, the small incidence angle causes high variations in the pixel size (from 60 to 10m in the range direction). For these two reasons, the parameters of the water class can not be considered constant in the image. It is also necessary to capture more local variations that result from the geometry of the scene or from wind variations.

In [8], we presented a method that used a quad-tree partitioning in order to obtain small regions where parameters could be supposed constant. While this approach accounts for global variations due to the uncorrected antenna pattern, it fails to capture variations at smaller scales. In this paper, we propose to alternatively optimize the classification (regularized through a MRF model) and a class parameter map defining the value of the class parameter at each pixel. This parameter map is also spatially regularized using a MRF.

The remainder of this paper is organized as follows. In section 2 the proposed method is described. In section 3, we present the datasets and experimental results of our method and compare them to some reference approaches. Finally, a discussion and some perspectives are presented in section 4.

2. METHOD

Detection of water in near-nadir incidence images is difficult because of the variations of water reflectivity in the image due

*Thanks to CNES and "Futur & Ruptures" program for funding.

in particular to varying windspeed and surface roughness, see Fig. 1(a) and (e). Detection of water areas therefore requires to estimate a map of water reflectivity jointly to the detection of water.

Starting from an observed SAR image v , our aim is to estimate the map of water reflectivity u and the detection of water areas w . The following paragraphs describe the image models proposed for those two unknown images u and w . Paragraph 2.3 then describes an algorithm to perform the joint estimation / detection.

2.1. Water reflectivity estimation

Due to the speckle phenomenon, the observed intensity v_i at pixel i in the water region of a SAR image is described by a multiplicative model:

$$v_i = u_i \cdot \xi_i, \quad (1)$$

where u_i is the water reflectivity at pixel i and ξ_i is the speckle that follows a Gamma distribution of unit mean. The log-transformed intensity $\tilde{v}_i = \log(v_i)$ is thus corrupted by an additive term $\tilde{\xi}_i$ that can be considered, in first approximation, as Gaussian distributed¹:

$$\tilde{v}_i = \tilde{u}_i + \tilde{\xi}_i \approx \tilde{u}_i + \tilde{\eta}_i, \quad (2)$$

with $\tilde{u}_i = \log u_i$, $\tilde{\xi}_i = \log \xi_i$ and $\tilde{\eta}_i$ Gaussian distributed.

Water reflectivity is expected to vary slowly in the azimuth direction, and more quickly in the range direction where it should follow quite closely the theoretical antenna diffraction pattern. Following an MRF modeling, we define the following Gaussian prior for water reflectivity \tilde{u} to account for these two types of variations:

$$-\log p(\tilde{u}) = \beta_{az} \sum_{i \sim_{az} j} (\tilde{u}_i - \tilde{u}_j)^2 + \beta_{rg} \sum_{i \sim_{rg} j} (\tilde{u}_i - \tilde{u}_j)^2 + \beta_{th} \sum_i (\tilde{u}_i - \tilde{p}_i)^2, \quad (3)$$

where $i \sim_{az} j$ denotes all pairs of pixels (i, j) that are neighbors in azimuth direction, $i \sim_{rg} j$ pairs of pixels that are neighbors in range direction, and $\tilde{p}_i = \log p_i$ is the log-transformed theoretical reflectivity given by the antenna diffraction pattern. Parameters β_{az} , β_{rg} and β_{th} are tuning parameters used to balance the importance of each term. Note that β_{th} can be set to 0 if the antenna pattern is not known.

A full map \tilde{u} of (log-transformed) water reflectivity can be obtained by maximum *a posteriori* estimation:

$$\arg \min_{\tilde{u}} \sum_i w_i \cdot (\tilde{u}_i - \tilde{v}_i)^2 + \beta_{az} \sum_{i \sim_{az} j} (\tilde{u}_i - \tilde{u}_j)^2 + \beta_{rg} \sum_{i \sim_{rg} j} (\tilde{u}_i - \tilde{u}_j)^2 + \beta_{th} \sum_i (\tilde{u}_i - \tilde{p}_i)^2, \quad (4)$$

¹a more accurate model is provided by Fisher-Tippett distribution, see [9]

with w the water detection map, *i.e.*, $w_i = 1$ if the pixel i belongs to water areas, $w_i = 0$ otherwise. Computation of the water detection map w is discussed in the following paragraph.

2.2. Water detection

While water areas backscatter strongly in the near-nadir incidence angles, ground areas backscatter much more weakly so that the observed intensity in ground areas is dominated by thermal noise: $\tilde{u}_i \approx \gamma$ for pixels i on the ground.

Since isolated ground pixels in water areas or isolated water pixels in ground areas are unlikely, we introduce an Ising regularization prior that penalizes such configurations for the detection map w :

$$-\log p(\tilde{w}) = \beta_{det} \sum_{i \sim j} \delta(\tilde{w}_i \neq \tilde{w}_j), \quad (5)$$

where $\delta(\tilde{w}_i \neq \tilde{w}_j) = 1$ if $\tilde{w}_i \neq \tilde{w}_j$ and $\delta(\tilde{w}_i \neq \tilde{w}_j) = 0$ if $\tilde{w}_i = \tilde{w}_j$, and β_{det} is a parameter to control the smoothness of the detection map.

For a fixed water reflectivity map u and a given level of noise γ , the optimal detection with respect to the MRF model is given by the following binary optimization problem:

$$\arg \min_{w \in \{0,1\}^N} \sum_i w_i \cdot (\tilde{u}_i - \tilde{v}_i)^2 + (1 - w_i) \cdot (\gamma - \tilde{v}_i)^2 + \beta_{det} \sum_{i \sim j} \delta(\tilde{w}_i \neq \tilde{w}_j), \quad (6)$$

where $i \sim j$ stands for all pairs (i, j) of neighboring pixels.

2.3. Proposed algorithm

The MRF formulations for the water reflectivity map and the detection map lead to optimization problems that can be efficiently solved one at a time. Optimization problem (4) is continuous and quadratic. It can be solved approximately by a few iterations of conjugate gradients. The estimation of the detection map with equation (6) requires to solve a binary optimization problem. This can be solved exactly by recasting the problem as a max-flow / min-cut problem [10]. We alternate both steps, leading to the following algorithm:

Algorithm for water detection

Input: SAR image v , thermal noise level γ ,
(optional) antenna diffraction pattern p

Output: detection map w

$\tilde{u} \leftarrow \log(p)$

do

$w \leftarrow$ compute solution of (6) by graph-cuts

$u \leftarrow$ compute solution of (4) by conjugate gradients

while w or u change

3. EXPERIMENTS

3.1. Data sets description

The proposed method is evaluated on both simulated and real data sets. The SWOT satellite is projected for launch in 2021, so only simulated images are currently available for evaluation. We use a simulation based on a Digital Elevation Model (DEM) of the Camargue area, France [11] shown in Figure 1(a). The azimuth resolution is 10m and the range resolution goes from 60 to 10m. Image size is 1839×2979 . This image features the uncorrected antenna pattern (see section 1) and local variations in the water radiometries (which are currently based on a gradient map).

To demonstrate that the method can be applied to multiple sensors, we also show some results on data acquired by SETHI (P-Band airborne sensor of ONERA) in HH polarization on Kaw, French Guiana. The amplitude image is shown in Figure 1(e). Azimuth resolution is 1.5m and slant-range resolution is 1.2m. The image size is 4000×5788 .

3.2. Experimental results

Model parameters selection: The proposed model is tuned by four parameters (β_{az} , β_{rg} , β_{th} , β_{det}) that depend on the amount of variations we choose to allow and on the scales of the objects we want to be able to detect. Results presented in the following paragraph have been computed using the following parameters:

- $\beta_{az} = 130$ and $\beta_{rg} = 500$ for both data sets;
- $\beta_{th} = 3$ for Camargue, $\beta_{th} = 1$ for Kaw;
- $\beta_{det} = 4$ for Camargue, $\beta_{det} = 10$ for Kaw.

We have to use a smaller β_{th} for Kaw as the antenna pattern was not known and could only be estimated. Also, due to the fact that the Kaw image has a finer resolution, higher regularization in the classification is required. However it can be seen that the parameters β_{az} and β_{rg} are the same for both images. The parameters tuning process therefore only depends on the resolution and the availability of the antenna pattern variation model, leading to a rather straightforward adaptation of the value of the parameters to new sensors.

Comparison with other methods: To demonstrate the effectiveness of our method, we compare it to the same model (Ising MRF with exact optimization) without the parameter map. We also compare to the method presented in [8] which also aims at finding a classification in image with varying parameters. Visual results are presented in Figure 1. The ground truth for the Camargue area has been obtained using the DEM from the simulation while it has been manually labeled for the Kaw data set. Note that for the Camargue area, we try to find water bodies (so a true positive is a water pixel labeled as a water pixel) while we are in a land vs. water configuration for the Kaw area.

| | Constant | NUMRF [8] | Proposed method |
|-----|-----------------|-----------------|-----------------|
| TPR | 78% / 99.00% | 78.64% / 99.14% | 92.98% / 98.25% |
| FPR | 0.27% / 21.30% | 0.17% / 7.45% | 1.12% / 3.31% |
| MCC | 0.85 / 0.87 | 0.86 / 0.93 | 0.92 / 0.95 |
| ER | 23.65% / 11.37% | 22.21% / 4.49% | 12.71% / 3.36% |

Table 1. Classification results for the Camargue and Kaw area

As could be expected, the method of [8] and the proposed method better capture spatial variations than the MRF with a constant parameter. While results from the proposed method and [8] are close on the Kaw data set (dominated by large scale variations), our method significantly improves [8] on the Camargue data set (displaying smaller scale variations).

These qualitative observations are confirmed by the quantitative evaluation available in Table 1. For each method, we report the True Positive Rate (TPR, higher is better), the False Positive Rate (FPR, lower is better), the Matthews correlation coefficient (MCC, higher is better) and the Error Rate (ER, lower is better) used in SWOT mission to define the scientific requirements. The MCC is defined as:

$$MCC = \frac{TP \times TN - FP \times FN}{\sqrt{(TP + FP)(TP + FN)(TN + FP)(TN + FN)}}, \quad (7)$$

and the Error Rate is defined as:

$$ER = \frac{FP + FN}{TP + FN}, \quad (8)$$

where TP, TN, FP and FN are True Positives, True Negatives, False Positives and False Negatives respectively.

Table 1 confirms the small improvement on the error rate and the MCC for Kaw area with the proposed method (expected as variations are of large scale), and the strong improvement over the Camargue area.

4. CONCLUSION

In this paper, a classification method for images with varying reflectivity parameters is proposed. It is based on a double Markov Random Field to jointly estimate the parameters and detect water. Visual and quantitative evaluation indicate that the proposed method outperforms a recently proposed technique. Our method seems promising both for airborne and satellite sensors. In the future, we will investigate the use of coherence and interferometric information, when available, to improve the results.

5. REFERENCES

- [1] R. Fjortoft et al., "KaRIn on SWOT: Characteristics of Near-Nadir Ka-Band Interferometric SAR Imagery," *Geoscience and Remote Sensing, IEEE Transactions on*, vol. 52, no. 4, pp. 2172–2185, April 2014.

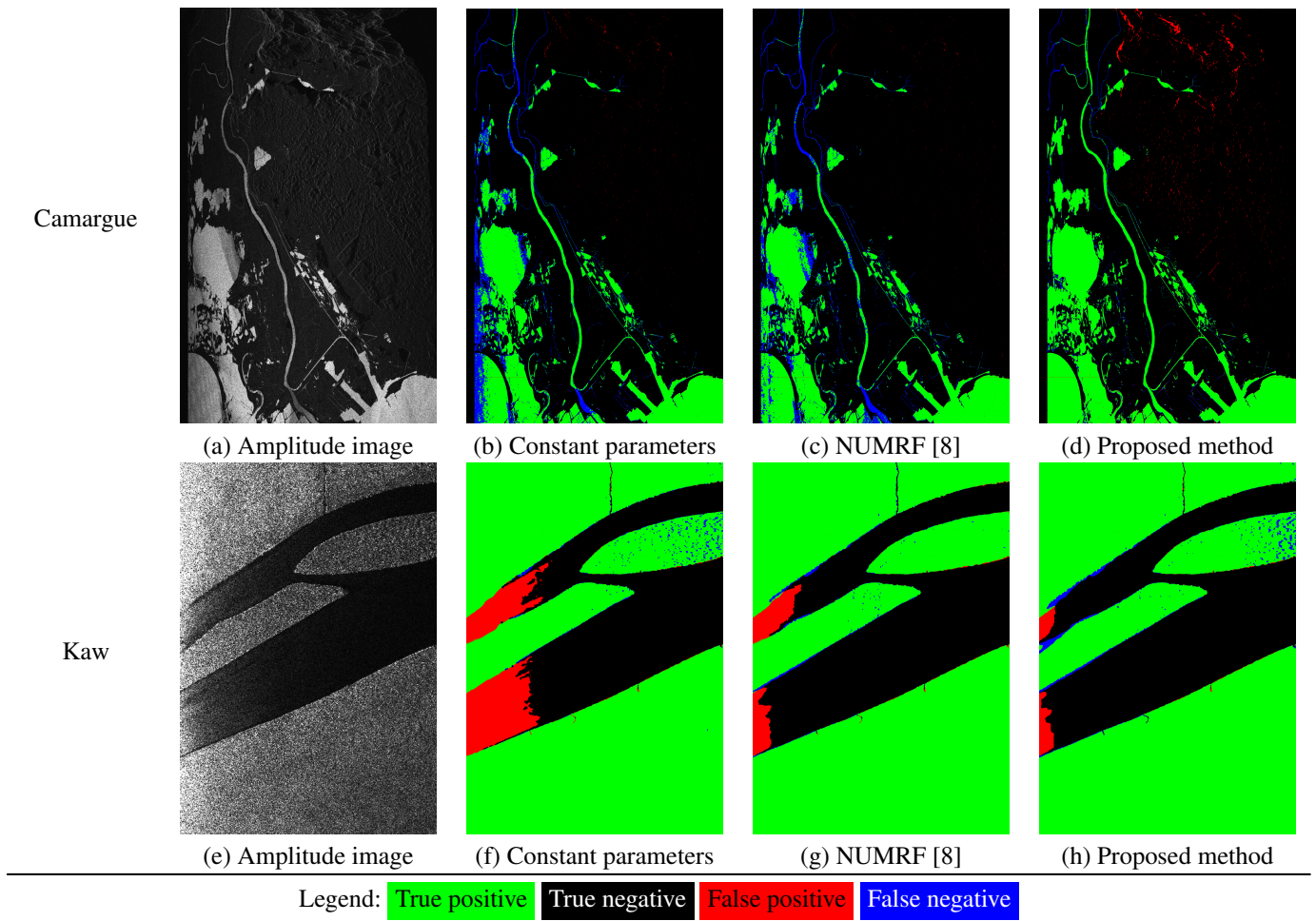


Fig. 1. Visual results on the data sets.

- [2] L. Pierce et al., “Knowledge-based classification of polarimetric SAR images,” *IEEE Transactions on Geoscience and Remote Sensing*, vol. 32, no. 5, pp. 1081–1086, 1994.
- [3] H. Liu et al., “A complete high-resolution coastline of antarctica extracted from orthorectified radarsat SAR imagery,” *Photogrammetric Engineering & Remote Sensing*, vol. 70, no. 5, pp. 605–616, 2004.
- [4] M. Silveira et al., “Separation between water and land in sar images using region-based level sets,” *IEEE Geoscience and Remote Sensing Letters*, vol. 6, no. 3, pp. 471–475, July 2009.
- [5] G. S. Xia et al., “Meaningful object segmentation from SAR images via a multiscale nonlocal active contour model,” *IEEE Transactions on Geoscience and Remote Sensing*, vol. 54, no. 3, pp. 1860–1873, March 2016.
- [6] C. Tison et al., “A new statistical model for Markovian classification of urban areas in high-resolution SAR images,” *Geoscience and Remote Sensing, IEEE Transactions on*, vol. 42, no. 10, pp. 2046–2057, 2004.
- [7] M. Bachmann et al., “TerraSAR-X antenna calibration and monitoring based on a precise antenna model,” *IEEE Transactions on Geoscience and Remote Sensing*, vol. 48, no. 2, pp. 690–701, 2010.
- [8] S. Lobry et al., “Non-uniform markov random fields for classification of SAR images,” in *EUSAR 2016*. VDE VERLAG GmbH, 2016.
- [9] J. Goodman, “Some fundamental properties of speckle,” *JOSA*, vol. 66, no. 11, pp. 1145–1150, 1976.
- [10] D. Greig et al., “Exact maximum a posteriori estimation for binary images,” *Journal of the Royal Statistical Society. Series B (Methodological)*, pp. 271–279, 1989.
- [11] J. Duro et al., “Simulation of near-nadir bistatic high resolution InSAR data in Ka-band for the SWOT mission,” in *EUSAR 2014; 10th European Conference on Synthetic Aperture Radar*, June 2014, pp. 1–4.